Communication

Design and Analysis of an Electronically Tunable Magnet-Free Non-Reciprocal Metamaterial

Swadesh Poddar, Alexander M. Holmes, and George W. Hanson

***Abstract*— In this communication, we develop and experimentally test a fully tunable magnet-free, non-reciprocal, split-ring resonator-based metamaterial. Non-reciprocity in the material response is introduced by bridging the split-ring gap with a biased field-effect transistor (FET) transistor, which allows the non-reciprocity to be tuned with respect to gate–source and drain–source bias conditions. As a measure of non-reciprocity, we consider the Faraday rotation of a normally incident linearly polarized planewave, which is a function of the co-polarized and cross-polarized *S*-parameters associated with two horn antennas that transmit and receive the wave. Faraday rotation is calculated with respect to the operating frequency of the horn antennas and manually measured with respect to drain–source current at the resonant frequency. Interestingly, we find a linear relationship between Faraday rotation and drain–source current at the resonance.**

***Index Terms*— Faraday rotation, metamaterial, non-reciprocity, ring resonators, tunability.**

I. Introduction

Wave–matter interactions may be subdivided into two broad categories, reciprocal and non-reciprocal [1]. When an electromagnetic wave exhibits the same propagation characteristics in the forward and reverse directions, the device or medium supporting the propagation is reciprocal. In the microwave regime of the electromagnetic spectrum, reciprocal devices have an *S*-parameter matrix that satisfies $\bar{\mathbf{S}} = \bar{\mathbf{S}}^{\mathrm{T}}$, where $\bar{\mathbf{S}}^{\mathrm{T}}$ is the transpose of $\bar{\mathbf{S}}$. By contrast, non-reciprocal devices exhibit different transmit to receive signal ratios when the transmit and receive ports are interchanged, leading to $\bar{\mathbf{S}} \neq \bar{\mathbf{S}}^{\mathrm{T}}$. At microwave frequencies, non-reciprocity has traditionally been implemented using ferrimagnetic materials (ferrites) magnetized with an external static magnetic bias field [2]. However, the use of magnetized ferrites in microwave devices has several disadvantages including weight, cost, footprint, and integrated circuit incompatibility [2].

Within the past decade, advances in metamaterial and semiconductor research have motivated an interest in magnet-free non-reciprocity, leading to novel technologies that mimic the response of magnetized ferrites without requiring an external magnetic bias. In a series of recent research works, Kodera *et al.* [3], [5], [6], Kodera and Caloz [4], and Sounas *et al.* [7] investigated the unidirectional properties of a field-effect transistor (FET) transistor in the design of a split-ring resonator based non-reciprocal metamaterial. On its own, a split-ring resonator is reciprocal and supports two counter propagating modes at the same resonant frequency that may be excited by right/left handed circular polarized (RHCP/LHCP) waves normally incident to the plane of the ring. However, when the gate and drain terminals of a biased FET transistor bridge the split-ring gap (source terminal grounded), the mode propagating from drain to gate is blocked, while the other propagating from gate to drain is allowed to pass. As a result, the ring resonates for only one type of circularly polarized wave, giving it a preferred handedness, and RHCP and LHCP waves propagate through the metamaterial with different phase velocities.

A linearly polarized wave may be expressed as the sum of two circularly polarized waves of opposite handedness and equal amplitude. If these two wave components propagate through a material with different phase velocities, the plane of polarization of the resultant linearly polarized wave rotates. While this process of polarization rotation can be reciprocal (e.g., in chiral materials that exhibit a reciprocal magneto-electric coupling [8]–[10]), it can also be non-reciprocal, in which case, the polarization rotation is referred to as Faraday rotation. In the case of Faraday rotation, the sign of rotation (i.e., clockwise or counterclockwise) is determined relative to the axis along which time-reversal (TR) symmetry is broken (e.g., in a magnetized ferrite, this axis would point parallel to the magnetization direction), whereas in chiral media exhibiting reciprocal magneto-electric coupling, the sign of rotation is determined relative to the propagation direction [11]; further details on the differences between nonreciprocal (Faraday) and reciprocal polarization rotation are provided in [1]. For the metamaterial first proposed in [3], and considered in this work, it is confirmed that wave propagation supported by the metamaterial is non-reciprocal, with Faraday rotation being the driving mechanism.

Building on the previous research work of Kodera *et al.* [3] we investigate the ability to tune the metamaterial response by means of variable gate–source (V_{GS}) and drain–source (V_{DS}) bias voltages that control the amount of dc current flowing between the drain and source terminals of an FET transistor (i.e., the drain–source current I_{DS}) that bridges the split-ring gap. Additionally, in contrast to the work in [3] and [6], we consider a measurement scheme based on transmission via the implementation of holes in the ground plane that is co-planar with each split-ring (i.e., this implementation makes the metamaterial transparent in the area enclosed by each split-ring). From the measured *S*-parameters, we calculate Faraday rotation, and confirm that wave propagation through the metamaterial is non-reciprocal by providing further evidence of isolation (i.e., $S_{21} \neq S_{12}$). Upon calculating Faraday rotation with respect to frequency for maximum drain–source current (i.e., at saturation), we proceed to manually measure Faraday rotation for decreasing values of I_{DS} by rotating the receive antenna polarization with respect to the transmitter until maximum transmission (i.e., maximum $|S_{21}|$) is achieved.

The communication is organized as follows. In Section II, we provide a detailed description of our metamaterial design. In Section III, we provide details regarding simulation, as well as a method for calculating Faraday rotation from simulated and measured *S*-parameters. In Section IV, we describe the measurement apparatus and present

Manuscript received 3 February 2021; revised 20 March 2022; accepted 21 March 2022. Date of publication 7 April 2022; date of current version 8 September 2022. This work was supported by the National Science Foundation under Grant EFMA-1741673. *(Corresponding author: Alexander M. Holmes.)*

The authors are with the Department of Electrical Engineering, University of Wisconsin at Milwaukee, Milwaukee, WI 53211 USA (e-mail: spoddar@uwm.edu; holmesam@uwm.edu; george@uwm.edu).

Color versions of one or more figures in this communication are available at https://doi.org/10.1109/TAP.2022.3164160.

Digital Object Identifier 10.1109/TAP.2022.3164160

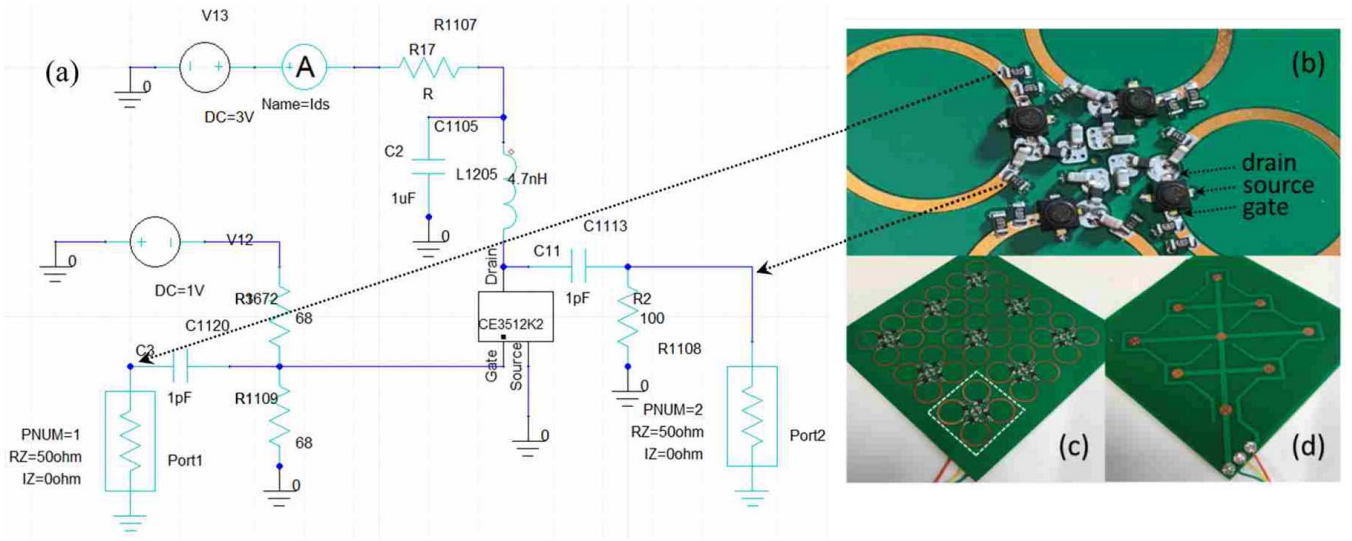

Fig. 1. (a) Circuit schematic of the lumped load, consisting of an FET and other passive elements, that bridges the split-ring gap, where ports labeled Port1 and Port2 correspond to each end of the split-ring. The load and split-ring comprise a single unit cell of the metamaterial, while the parallel connection of four unit cells comprise a single supercell having fourfold symmetry with respect to the surface normal. (b) Zoomed-in view of a single supercell corresponding to the dashed outline on the front side of the board shown in (c). (d) Backside of a 3 × 3 supercell board having a total dimension of 90 mm × 90 mm. Each supercell of the metamaterial is connected in parallel, allowing the dc bias to be applied at a common location (i.e., corner), with colored wires soldered to three points corresponding to gate (red), drain (green), and source (yellow).

our measured results in comparison with those obtained from simulation.

II. Principle of Operation

The metamaterial design considered in this work is a modest extension of the one first proposed in [3], that being a periodic array of microstrip split-ring resonators with the gate and drain bias terminals of an FET transistor bridging the split-ring gap, and a ground plane that is co-planar with the split-ring array. In the unbiased case, the split-ring supports two counterpropagating guided modes at the resonant frequency that are excited by RHCP and LHCP electromagnetic waves normally incident to the plane of the ring. Once biased, the mode propagating from drain to gate is blocked, while the other propagating from gate to drain is allowed to pass, making the ring resonant for only one type of circular polarization, which gives the metamaterial a preferred handedness, irrespective of the propagation direction. As a result, TR symmetry in the effective response of the medium is broken along a constant axis perpendicular to the plane of the ring, rendering the metamaterial response nonreciprocal.

The resonant frequency at which the excitation of guided modes on the split-ring occurs is set by the physical dimension (i.e., the inner radius R) of the ring. When an integer number n of guided wavelengths $\lambda_g = \lambda_0/\sqrt{\varepsilon_e}$ is equal to the circumference, the resonance condition (i.e., $n\lambda_g = 2\pi R$) is met, where λ_0 is the freespace wavelength and ε_e is the effective (relative) permittivity of the microstrip geometry [12]

$$\varepsilon_e = \frac{\varepsilon_r + 1}{2} + \frac{\varepsilon_r - 1}{2}\frac{1}{\sqrt{1 + 12d/W}} \tag{1}$$

with W, d, and ε_r denoting the strip width, substrate height, and relative permittivity of the substrate respectively. In what follows, the inner radius of the split-ring is chosen such that the $n = 1$ resonant frequency occurs at 7.165 GHz. For optimal results, it is important that the characteristic impedance of the split-ring be matched to that of the load bridging the gap in order to minimize the standing wave ratio on the ring. To calculate the characteristic impedance Z_0, we use [12]

$$Z_0 = \frac{120\pi}{\sqrt{\varepsilon_e}\,[W/d + 1.393 + 0.667\ln(W/d + 1.444)]} \tag{2}$$

such that $W/d > 1$, $d = 0.8$ mm, and $\varepsilon_r = 4.35$ which corresponds to an FR4-TG-140 substrate. The strip width is then varied accordingly to match the load impedance.

Fig. 1(a) shows the lumped load consisting of an FET transistor and other passive elements (i.e., resistors, inductors, and capacitors) connected across two ports (labeled Port1 and Port2) corresponding to the two ends of the split-ring. Coupling capacitors C3 and C11, connected to the gate and drain respectively, block the flow of dc current on the ring while passing ac current (excited via normally incident electromagnetic waves) to the gate and drain. The amount of ac current allowed to pass from gate to drain is then tunable via the dc drain–source current, while the flow of ac current in the reverse direction (i.e., from drain to gate) is blocked. A voltage divider implemented at the gate using resistors labeled R3672 and R1109 allows V_{GS} to be tuned for various bias conditions obtained from the I–V characteristic curve of the FET. The inductor labeled L1205 blocks RF signals from entering the source (in general, the associated reactance should be well beyond 500 Ω at resonance), while the bypass capacitor labeled C2 filters any additional ac noise to ground. Resistor R2 is solely used for impedance matching purposes, while resistor R17 is used in conjunction with ammeter Ids to probe the dc current (this is for simulation purposes only, not included in the fabricated board) drawn from voltage supply V13 connected to the drain that ultimately flows to the source (i.e., the dc drain–source current). To optimize performance, values for all passive elements are selected during a full-wave simulation using the pattern search algorithm in HFSS. For ease of assembly and precise performance, the surface mount elements are selected with high Q, low loss, and low tolerance.

The load and split-ring comprise a single unit cell of the metamaterial, while the parallel connection of four unit cells forms a supercell having fourfold symmetry with respect to the surface normal. Front

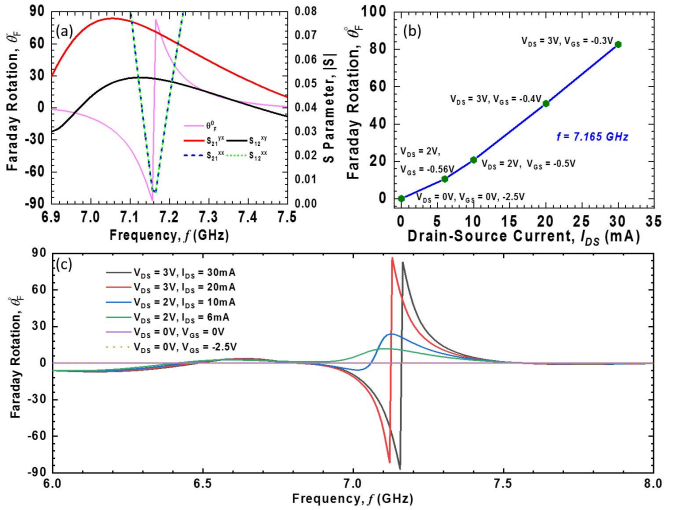

Fig. 2. (a) Simulated S-parameter coefficients (right vertical axis) alongside the calculated Faraday rotation (left vertical axis) for $I_{\mathrm{DS}} = 30$ mA. (b) Calculated Faraday rotation shown to vary in a linear fashion with respect to I_{DS} at the resonant frequency $f = 7.165$ GHz associated with $I_{\mathrm{DS}} = 30$ mA. (c) Calculated Faraday rotation for several values of I_{DS} in the range of 0 to 30 mA.

and backside views of the fabricated board are shown in Fig. 1(c) and (d), with a zoomed-in view of the supercell shown in Fig. 1(b). The parallel connection of each unit cell allows the dc bias to be applied in one location (i.e., corner) of the board, shown in Fig. 1(d), with colored wires soldered to three points corresponding to gate (red), drain (green), and source (yellow), and conductive traces extending from the common gate and drain biasing points to each unit cell. The ground plane, co-planar with each split ring, exists everywhere, except in the area enclosed by each ring (i.e., in these areas, the metamaterial is transparent). The green resin coating the metamaterial is a solder mask which protects against oxidation. Additional perspective views of the metamaterial depicted in the simulation environment are provided in the Appendix, with labels attached to several key features just mentioned.

III. Simulation

To model Faraday rotation, we consider a monochromatic linear polarized transverse electromagnetic wave normally incident on the metamaterial, which may be written as the sum of two circular polarized waves of opposite handedness and equal amplitude

$$\mathbf{E}_i = \hat{\mathbf{a}} E_0 e^{-j\mathbf{k}\cdot\mathbf{r}} = \frac{\hat{\mathbf{a}}_{\circlearrowright} + \hat{\mathbf{a}}_{\circlearrowleft}}{\sqrt{2}} E_0 e^{-j\mathbf{k}\cdot\mathbf{r}} \tag{3}$$

where

$$\hat{\mathbf{a}}_{\circlearrowright,\circlearrowleft} = \frac{\hat{\mathbf{a}} \mp j\hat{\mathbf{k}} \times \hat{\mathbf{a}}}{\sqrt{2}} \tag{4}$$

are unit polarizations for RHCP and LHCP waves respectively, defined in terms of the unit linear polarization $\hat{\mathbf{a}}$ and wavevector $\mathbf{k} = \hat{\mathbf{k}} k_0$, with $k_0 = 2\pi/\lambda_0$. The transmitted field $\mathbf{E}_t = \bar{\mathbf{T}} \cdot \mathbf{E}_i$ is defined generally in terms of the transmission tensor

$$\bar{\mathbf{T}} = \hat{\mathbf{a}}\hat{\mathbf{a}} T_{\parallel} + \hat{\mathbf{k}} \times \hat{\mathbf{a}}\hat{\mathbf{a}} T_{\perp} \tag{5}$$

where the coefficients $T_{\parallel}$ and $T_{\perp}$ are associated with the transmitted field components that are parallel (co-polarized) and orthogonal (cross-polarized) to the incident field respectively. Similarly, the transmitted field, decomposed into RHCP and LHCP waves, is obtained

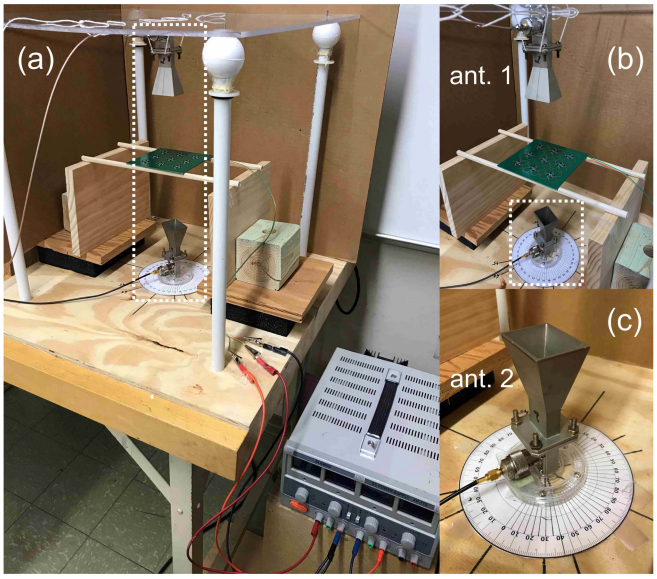

Fig. 3. (a) Measurement apparatus with mounted horn antennas, one polarization fixed (ant. 1) and the other variable (ant. 2). The metamaterial is placed equidistant between the two antennas in the far-field. The power supply used to bias the gate and drain terminals of transistors in the metamaterial is shown bottom right. (b) Zoomed-in view of dashed section outlined in (a). (c) Zoomed-in view of dashed section outlined in (b) shows antenna 2 mounted on a Lazy Suzan with a protractor used to measure the rotation angle with respect to the co-polarized state.

via the unitary transformation $\mathbf{E}'_t = \mathbf{U}^{\dagger} \cdot \mathbf{E}_t$, where $\mathbf{U}^{\dagger}$ is the complex transpose of

$$\mathbf{U} = \left(\frac{\hat{\mathbf{a}} - j\hat{\mathbf{k}} \times \hat{\mathbf{a}}}{\sqrt{2}}\right)\hat{\mathbf{a}}_{\circlearrowright} + \left(\frac{\hat{\mathbf{a}} + j\hat{\mathbf{k}} \times \hat{\mathbf{a}}}{\sqrt{2}}\right)\hat{\mathbf{a}}_{\circlearrowleft} \tag{6}$$

and

$$\mathbf{E}'_t = \left[\hat{\mathbf{a}}_{\circlearrowright} T_{\circlearrowright} + \hat{\mathbf{a}}_{\circlearrowleft} T_{\circlearrowleft}\right] E_0 e^{-j\mathbf{k}\cdot\mathbf{r}} \tag{7}$$

where $T_{\circlearrowright/\circlearrowleft} = T_{\parallel} \pm jT_{\perp}$. Faraday rotation is then defined as 1/2 the phase difference between RHCP and LHCP transmitted field components [8]

$$\theta_F = \left[\arg\left(T_{\circlearrowright}\right) - \arg\left(T_{\circlearrowleft}\right)\right]/2. \tag{8}$$

As explained in the previous section, the degree of Faraday rotation is tunable by varying the dc drain–source current I_{DS}. Using Ansys HFSS, a full wave simulation and floquet mode analysis is performed on a single supercell of the metamaterial to obtain the necessary transmission coefficients (i.e., S-parameters). In the simulation and experiment, we take $\hat{\mathbf{k}} = \hat{\mathbf{z}}$ from antenna 1 to antenna 2, and $\hat{\mathbf{a}} = \hat{\mathbf{x}}$. Fig. 2(a) shows the magnitude of the simulated transmission coefficients $T_{\parallel} = S_{21}^{xx}$ and $T_{\perp} = S_{21}^{yx}$ (right vertical axis) alongside the calculated Faraday rotation (left vertical axis) for $I_{\mathrm{DS}} = 30$ mA. Also shown, are the coefficients obtained when the ports and polarizations are interchanged (i.e., $S_{21}^{yx} \rightarrow S_{12}^{xy}$ and $S_{21}^{xx} \rightarrow S_{12}^{xx}$). A nonzero isolation, defined as the difference in S-parameter magnitude (i.e., $|S_{21}^{xy}| - |S_{12}^{yx}|$ and $|S_{21}^{xx}| - |S_{12}^{xx}|$), is a signature of nonreciprocal wave propagation through the metamaterial.

Fig. 2(c) shows the calculated Faraday rotation from simulated S-parameters for several values of I_{DS} that decrease from 30 mA to 0. At the resonant frequency $f = 7.165$ GHz associated with $I_{\mathrm{DS}} = 30$ mA, Faraday rotation decreases in a linear fashion with respect to I_{DS}, as shown in Fig. 2(b).

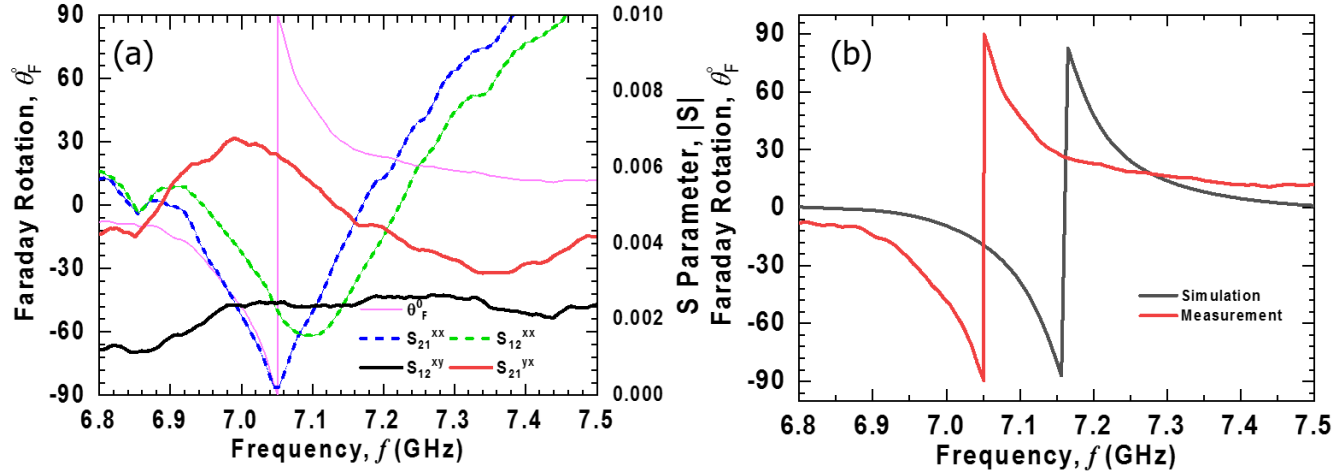

Fig. 4. (a) Measured S-parameter coefficients (right vertical axis) alongside the calculated Faraday rotation (left vertical axis) for $I_{DS} = 30$ mA. At the resonant frequency, $f = 7.05$ GHz, a large amount of isolation occurs in the cross-polarized coefficients, a signature of nonreciprocal wave propagation through the metamaterial. The measured S-parameters and calculated Faraday rotation follow the same trend observed in simulation as shown in Fig. 2(a). (b) Comparison of the calculated Faraday rotation obtained using simulated and measured S-parameters. The resonant frequency differs by ∼1.6%.

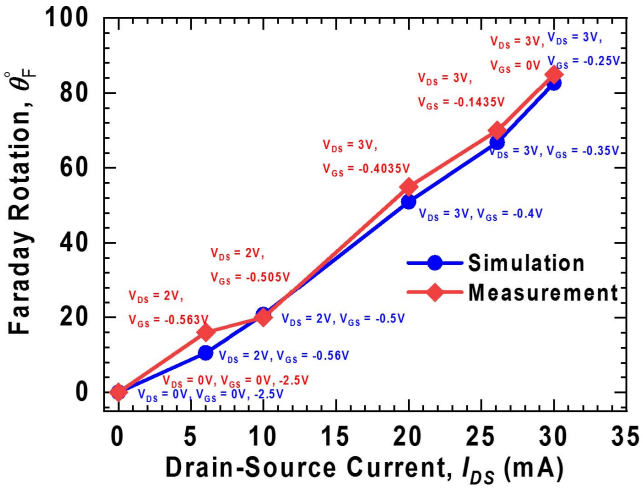

Fig. 5. (a) Variation of simulated and measured Faraday rotation with respect to the drain–source current at each of the associated resonant frequencies corresponding to $I_{DS} = 30$ mA (i.e., for measurement, $f = 7.05$ GHz, and for simulation, $f = 7.165$ GHz). The gate and drain bias settings to realize each value of drain–source current are also noted next to each data point.

IV. Measurement

Fig. 3(a)–(c) shows different perspective views of the apparatus used to measure the co-polarized and cross-polarized transmission coefficients of two horn antennas (labeled ant. 1 and ant. 2) having an operational frequency range of 6.5 to 12 GHz. The fabricated metamaterial is placed equi-distant between the antennas in the far-field, and S-parameters are measured using a vector network analyzer. At the resonant frequency associated with $I_{DS} = 30$ mA, peak Faraday rotation is measured manually for several values of I_{DS} by rotating antenna 2 (initially co-polarized along $\hat{\mathbf{x}}$) until maximum transmission (i.e., maximum $|S_{21}|$) is achieved. A measureable rotation angle, corresponding to the measured value of Faraday rotation, is realized by implementing the setup shown in Fig. 3(c) consisting of a protractor and Lazy Susan. Prior to the manual measurement, the resonant frequency associated with $I_{DS} = 30$ mA is numerically extracted from the Faraday rotation calculation, performed using (8) for the measured co-polarized and cross-polarized transmission coefficients over the frequency range of operation.

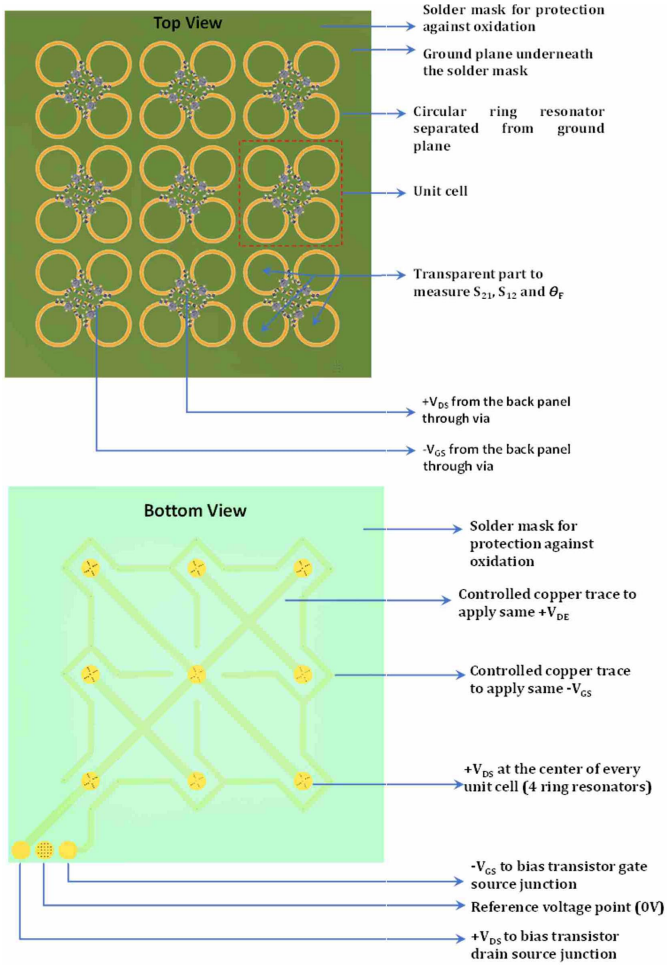

Fig. 6. Top and bottom side views of the metamaterial.

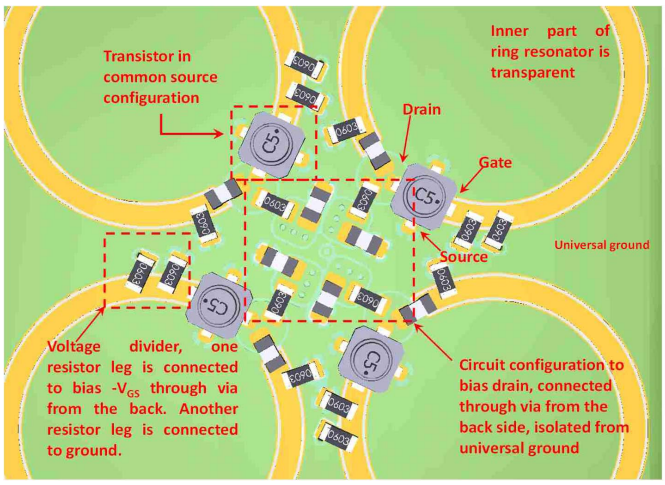

Fig. 7. Circuit configuration showing assembled SMD components.

Fig. 4(a) shows the measured S-parameter coefficients S_{21}^{xx}, S_{12}^{xx}, S_{21}^{yx}, and S_{12}^{xy} (right vertical axis) alongside the calculated Faraday rotation (left vertical axis) for $I_{\mathrm{DS}} = 30$ mA. Variation in the S-parameter measurements with respect to frequency is similar to the simulated results shown in Fig. 2(a), with $|S_{21}^{yx}|$ nearly maximum at the resonant frequency $f = 7.05$ GHz, and $|S_{21}^{xx}|$ minimum. In addition, a comparable amount of isolation is found, confirming that wave propagation through the metamaterial is nonreciprocal. Lastly, we note that transmission levels are roughly one order of magnitude less than those obtained in simulation due to a combination of substrate loss and a slight overlap of the gate and drain copper traces with the transparent areas of the board, which we did not account for in the simulation. The optimized placement of these traces would certainly result in higher transmission. In Fig. 4(b), Faraday rotation calculated from S-parameters obtained in simulation and measurement are shown. The extracted resonant frequencies in each case differ by $\sim$1.6%, likely due to variation in the substrate permittivity ε_r with respect to frequency (i.e., our simulation and performance evaluation is based on the measured value of ε_r at 500 MHz, provided by the manufacturer).

Having obtained the resonant frequency experimentally for $I_{\mathrm{DS}} = 30$ mA, a manual measurement of Faraday rotation is performed at resonance where I_{DS} is reduced gradually from 30 mA to 0. As I_{DS} decreases, the angle through which antenna 2 rotates with respect to antenna 1 to achieve maximum $|S_{21}|$ (i.e., the Faraday rotation angle) decreases in a linear fashion, and compares well with the results obtained from simulation as shown in Fig. 5. In the figure, the gate and drain bias conditions associated with each value of I_{DS} from simulation and measurement are also noted next to each data point.

V. Conclusion

In this work, we present a detailed analysis of a fully tunable non-reciprocal metamaterial inspired by a previous split-ring resonator design. The metamaterial design along with the necessary setup conditions are proposed and demonstrated to measure tunable Faraday rotation with respect to the drain–source current of an FET transistor that bridges the split-ring gap. From the results, we conclude that electronically tunable nonreciprocal metamaterials may serve as a practical substitute for conventional ferrimagnetic materials in nonreciprocal microwave devices. Our hope is that this work will add a new building block in the existing research area of magnet-free non-reciprocity.

Appendix

Fig. 6 shows the front and backsides of the metamaterial in the simulation environment with labels pointing to several key features described in Section II including the solder mask, universal ground plane, and conductive traces that stem from the common biasing location to the center of each supercell. In addition, a zoomed-in view of the supercell on the front side of the board, corresponding to the dashed outline in Fig. 6, is shown in Fig. 7 with labels pointing to the various surface mount device (SMD) components of the load schematic shown in Fig. 1. In a common source configuration, the gate is biased with a negative voltage $-V_{\mathrm{GS}}$ with respect to ground while the drain is biased with a positive voltage $+V_{\mathrm{DS}}$.

Acknowledgment

The authors would like to thank Christophe Caloz, Toshiro Kodera, Tanvir Hasan, Mohsen Sabbaghi, and Salahuddin Tariq for helpful discussions and guidance, and ANSYS for providing access to their learning hub platform. In addition, we recognize 3dphotonics for fabricating the designed metamaterial.

References

[1] C. Caloz, A. Alù, S. Tretyakov, D. Sounas, K. Achouri, and Z.-L. Deck-Léger, "Electromagnetic nonreciprocity," *Phys. Rev. Appl.*, vol. 10, no. 4, Oct. 2018, Art. no. 047001.
[2] A. Kord, D. L. Sounas, and A. Alù, "Microwave nonreciprocity," *Proc. IEEE*, vol. 108, no. 10, pp. 1728–1758, Oct. 2020.
[3] T. Kodera, D. L. Sounas, and C. Caloz, "Artificial Faraday rotation using a ring metamaterial structure without static magnetic field," *Appl. Phys. Lett.*, vol. 99, no. 3, Jul. 2011, Art. no. 031114.
[4] T. Kodera and C. Caloz, "Unidirectional loop metamaterials (ULM) as magnetless artificial ferrimagnetic materials: Principles and applications," *IEEE Antennas Wireless Propag. Lett.*, vol. 17, no. 11, pp. 1943–1947, Nov. 2018.
[5] T. Kodera, D. L. Sounas, and C. Caloz, "Magnetless nonreciprocal metamaterial (MNM) technology: Application to microwave components," *IEEE Trans. Microw. Theory Techn.*, vol. 61, no. 3, pp. 1030–1042, Mar. 2013.
[6] T. Kodera, D. L. Sounas, and C. Caloz, "Switchable magnetless nonreciprocal metamaterial (MNM) and its application to a switchable Faraday rotation metasurface," *IEEE Antennas Wireless Propag. Lett.*, vol. 11, pp. 1454–1457, 2012.
[7] D. L. Sounas, T. Kodera, and C. Caloz, "Electromagnetic modeling of a magnetless nonreciprocal gyrotropic metasurface," *IEEE Trans. Antennas Propag.*, vol. 61, no. 1, pp. 221–231, Jan. 2013.
[8] I. Lindell, A. Sihvola, S. Tretyakov, and A. Viitanen, *Electromagnetic Waves in Chiral and Bi-Isotropic Media*. Norwood, MA, USA: Artech House, 1994.
[9] B. Wang, J. Zhou, T. Koschny, M. Kafesaki, and C. M. Soukoulis, "Chiral metamaterials: Simulations and experiments," *J. Opt. A, Pure Appl. Opt.*, vol. 11, no. 11, Sep. 2009, Art. no. 114003.
[10] S. Zhang *et al.*, "Photoinduced handedness switching in terahertz chiral metamolecules," *Nature Commun.*, vol. 3, no. 1, p. 942, Jan. 2012.
[11] D. Floess *et al.*, "Tunable and switchable polarization rotation with nonreciprocal plasmonic thin films at designated wavelengths," *Light, Sci. Appl.*, vol. 4, no. 5, p. e284, May 2015.
[12] D. Pozar, *Microwave Engineering*, 4th ed. Hoboken, NJ, USA: Wiley, 2011.